https://doi.org/10.1016/j.applthermaleng.2020.114959

Three-dimensional modeling of flow field optimization for co-electrolysis solid oxide electrolysis cell

Yang Wang[1,a], Yingmeng Du[1,a], Meng Ni[b], Ruobing Zhan[a], Qing Du[a,*], Kui Jiao[a,*]

[a]State Key Laboratory of Engines, Tianjin University,

135 Yaguan Road, Tianjin, China, 300350

[b]Building Energy Research Group, Department of Building and Real Estate,

The Hong Kong Polytechnic University, Hung Hom, Kowloon, Hong Kong, China

*Corresponding author: kjiao@tju.edu.cn (K. Jiao); duqing@tju.edu.cn (Q. Du)

tel: +86-22-27404460; fax: +86-22-27383362

Abstract

Flow field optimization has an evident effect on the performance improvement of solid oxide electrolysis cells (SOEC). In this study, a novel flow field based on porous material is proposed to improve the electrolysis efficiency of SOEC. The internal reforming reactions, multi-component diffusion process and co-electrolysis of H_2O and CO_2 are numerically studied by establishing a three-dimensional model. The results show that the novel design with porous material instead of conventional rib-channel configuration can lower the electrolysis voltage demand up to 0.062V. To understand the mechanisms for the improved performance of the new flow field design, the multi-physical field distributions and thermal process are investigated. It is found that the new flow field design can ensure more uniform distribution of species concentration and reduce the maximum temperature difference by 3.81K at 1.5A cm^{-2}. The thermal analysis indicates that the ohmic loss is the most important factor for temperature distribution. In addition, the structure and configuration of porous flow field are further optimized to obtain a better performance.

Keywords: Co-electrolysis SOEC; Three-dimensional model; Flow field optimization; Porous material; Cell performance.

Nomenclature

A_{act}	active area, m^2
c_p	specific heat capacity, kJ kg^{-1} K^{-1}
D	gas diffusivity, m^2 s^{-1}
E_{input}	electrical power consumption, W m^{-2}
E_r	open circuit voltage, V
F	faraday's constant, C mol^{-1}
H	internal reforming heat, J mol^{-1}
J	current density, A m^{-2}
j	exchange current density, A m^{-3} or species j
k	Knudsen
K_{pr}	equilibrium constant of MSR
K_{ps}	equilibrium constant of WGSR
k_{rf}	forward reaction rate constant for MSR
k_{sf}	forward reaction rate constant for WGSR
L	length, mm
M	molecular weight, kg mol^{-1}
n	mole flow rate, mol s^{-1}
n_e	number of electrons transferred per reaction

p	gas pressure, Pa or atm
R	universal gas constant, J mol^{-1} K^{-1}
r	pore radius, μm
S	source term, kg m^{-3} s^{-1}, mol m^{-3} s^{-1} or W m^{-3}
T	temperature, K
t	time, s
u_f	fuel utilization
V	special Fuller diffusion volume, cm^{-3} mol^{-1}
V_{demand}	voltage demand for electrolysis, V
W	width, mm
x	mole fraction
y	mass fraction

Greek letters

0	standard state
α	transfer coefficient in anode
β	transfer coefficient in cathode
δ	thickness, m
ε	porosity
ξ	air stoichiometric ratio
φ_{ele}	electric potential, V
φ_{ion}	ionic potential, V
γ	adjustable parameter

η	overpotential, V, or electrolysis efficiency
κ	thermal conductivity, W m^{-1} K^{-1}
σ	conductivity, S m^{-1}
μ	viscosity, kg m^{-1} s^{-1}
v	velocity, m s^{-1}
ρ	density, kg m^{-3}
τ	tortuosity
ω	volume fraction of electron conducting particles

Subscripts and superscripts

a	anode
act	activation
c	cathode
che	chemical
eff	effective
ele	electron
i	gas species
ion	ion
irr	irreversible
k	reaction order for oxygen
m	reaction order for hydrogen
n	reaction order for carbon monoxide
ohm	ohmic

ref	reference state
rev	reversible
u	momentum

Abbreviations

ACL	anode catalyst layer
ADL	anode diffusion layer
AEC	alkaline electrolysis cell
CCL	cathode catalyst layer
CDL	cathode diffusion layer
LHV	lower heat value
MSR	methane steam reforming reaction
PEMFC	proton exchange membrane fuel cell
PEN	positive electrode-electrolyte-negative electrode
SOCs	solid oxide cells
SOEC	solid oxide electrolysis cell
SOFC	solid oxide fuel cell
UDF	user defined functions
WGSR	water gas shift reaction

1. Introduction

In recent years, much interest has been focused on the renewable and eco-friendly power resources due to the increasing energy demand and global environmental concerns [1].

Meanwhile, the meteorological fluctuations of these renewable energies (e.g. solar and wind energy) and the redundant electricity in power grid provide a promising opportunity for energy conversion and storage techniques [2]. Among these techniques, the solid oxide electrolysis cell (SOEC), which is a reversed mode of solid oxide fuel cell (SOFC), has aroused much attention for its high efficiency and low emission [3,4].

Unlike some other types of electrolysis devices, such as proton exchange membrane electrolysis cell (PEMEC) and alkaline electrolysis cell (AEC), SOEC operates at high temperature (typically between 873 and 1073K) and can achieve a lower voltage demand [5]. Besides, this technology can also offer an approach to directly electrolyze CO_2 [6]. For these reasons, the co-electrolysis of SOEC provides a promising pathway for energy storage and transport. As it is expensive and challenging to investigate these complicated processes by experimental measurements, numerical modeling and simulation become particularly important as an efficient and low-cost tool.

Numerous numerical simulations have been conducted to investigate the effects of flow field geometry on the performance of fuel cells [7-10]. Various types of flow fields are designed, i.e., parallel, serpentine and interdigitated flow fields, and so on [11-13]. One of the key problems during PEMFC operation is the removal of condensed liquid water, which is also the purpose of flow field optimization [14]. In contrast, there is no liquid water inside solid oxide cells (SOCs) because of the high working temperature. But flow field optimization is still needed for large-scale application due to the highly non-uniform distribution of the temperature, gas concentration, current density etc. Thereinto, significant research efforts have been made to improve the flow uniformity to improve the overall cell performance and durability. Duhn et al. [15] designed a special gas distributor with a flow uniformity index of 0.978. Bi et al. [16] found that the key factor affecting the flow uniformity of SOFC stack is the ratio of intake manifold width to outlet manifold width. Lin et al. [17] established a three-dimensional model of SOFC stack, and put forward a quantitative index to evaluate the flow uniformity. Dong et al. [18] designed a novel manifold for gas distribution in fuel cell stack, and this structure could achieve a uniformity of 0.99. At the same time, many researchers further improved the cell thermal distribution by optimizing the flow field structure. Qu et al. [19] adopted corrugated bipolar plates as channels, and a relatively low temperature

difference was found. They also found that considering the radiation heat can accomplish more accurate prediction on temperature field. Wei et al. [20] proposed a new hexagonal SOFC design for multi-cell stack arrangement to reduce the thermal stress of stack. It should be noted that they tried to change the cathode channel to porous material, and the modified cell performed a better output performance.

The root problem for the thermal-fluid-electrical non-uniform distribution lies in the traditional flow field structure which consists of ribs and channels. Several numerical models were established to figure out the effects of rib on gas transport and identified the optimal rib structure [21-25]. But these attempts cannot completely solve the problem. However, the porous material flow field can overcome this obstacle. For porous material flow field, the ribs and channels are replaced by a porous component which can be metal foam or porous cermet. Metal foam has been widely used in PEMFC, and extensive researches are reported that the metal foam can significantly improve the cell performance [26-29]. But for SOCs, the oxygen electrode operates in a strongly high-temperature oxidizing atmosphere, and such operating conditions raise higher requirements for adopting this porous structure. Recently, Zielke et al. [30] experimentally studied the cell degradation characteristics adopting Cu-Mn foam as oxygen electrode contact material. The test results show that the Cu-Mn foam is sufficient to allow the cell to operate for longer than 350 h, and this metal foam presents itself as an effective structure to enhance the oxygen electrode conductivity of SOCs. This proves that the porous material flow field is an effective structure to improve cell performance.

But these studies mentioned above are focused on SOFC. Some researchers have reported that the heat transfer processes of SOEC differ from that of SOFC [31]. For example, unlike SOFC normally running in exothermic mode, the operation of SOEC can be endothermic, exothermic or thermoneutral. And the relevant conclusions drawn from SOFC models are not accurate to predict the performance of SOEC. Although SOEC can be regarded as the reverse mode of SOFC, the mass and current transport direction are completely different. But to the best of authors' knowledge, there is a notable paucity of studies focusing on the flow field design of SOEC, which can significantly optimize the transmission path of species and current to reach a better electrolysis efficiency. Considering the significance of thermal-fluid-electrical distribution on electrolysis performance, flow field design and optimization for

SOEC will be of great interest.

In this study, a three-dimensional single cell model, considering the co-electrolysis of water and carbon dioxide, internal reforming reactions and multi-component diffusion, is developed to predict the cell performance of a cathode-supported planar SOEC. A novel porous material flow field design is proposed and compared with three traditional multi-channel flow fields (parallel, serpentine and parallel serpentine) in detail. Moreover, the structure optimization for porous flow field is performed to obtain the most suitable configuration.

2. Model development

Fig.1 illustrates the schematics of a planar cathode-supported SOEC utilized in this study. The computational domain mainly constitutes by three parts: anode/cathode interconnects, PEN (positive electrode-electrolyte-negative electrode) and anode/cathode channels. Among them, for traditional flow field, the multi-entry channels exist between the anode/cathode interconnects and the PEN, and the flow configuration is counter-flow by default. The PEN consists of ACL/CCL (anode/cathode catalyst layer), ADL/CDL (anode/cathode diffusion layer) and electrolyte. The dense electrolyte is sandwiched between the thin porous anode electrode and thick porous cathode electrode.

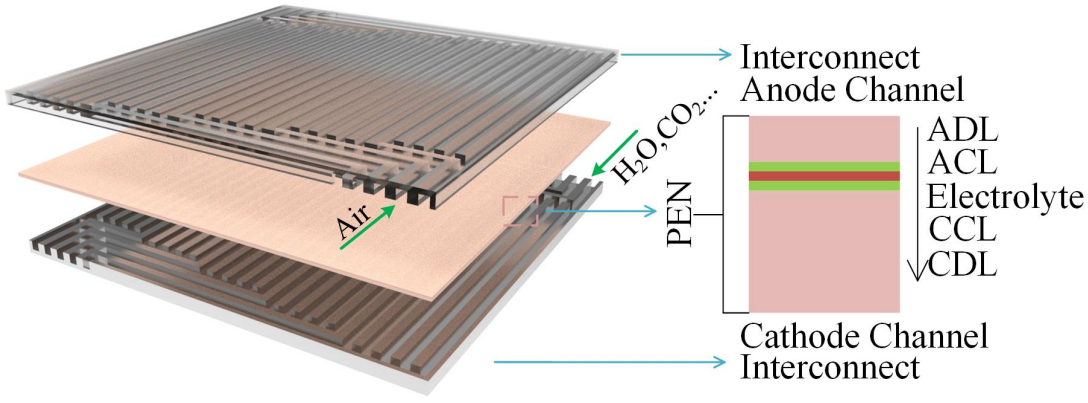

Fig. 1 The schematics of a planar cathode-supported SOEC.

As shown in Fig. 1, a mixture of H_2O, CO_2 and H_2 is supplied to cathode channel, then the high operating temperature induces internal reforming reactions, which include reversible

119 water gas shift reactions (WGSR) and methane steam reforming reactions (MSR). The
120 reactions can be expressed as follows:

$$CO + H_2O \leftrightarrow CO_2 + H_2 \quad \text{(WGSR)} \tag{1}$$

$$CH_4 + H_2O \leftrightarrow CO + 3H_2 \quad \text{(MSR)} \tag{2}$$

121 Meanwhile, H_2O and CO_2 diffuse into the CCL where the co-electrolysis reactions occur.
122 Then the generated oxygen ions are transported to anode side through electrolyte layer. The
123 electrochemical reaction process can be expressed as follows:

$$CO_2 + 2e^- \rightarrow CO + O^{2-} \quad \text{(cathode)} \tag{3}$$

$$H_2O + 2e^- \rightarrow H_2 + O^{2-} \quad \text{(cathode)} \tag{4}$$

$$O^{2-} \rightarrow 1/2\,O_2 + 2e^- \quad \text{(anode)} \tag{5}$$

124 ## *2.1 Conservation equations*

125 Conservation equations are included in the model to represent the mass and heat transfer
126 process and electrochemical reaction kinetics inside the electrolysis cell. All the conservation
127 equations are summarized in Table 1, while the source terms of these conservation equations
128 are provided in Table 2. It should be mentioned that the porosity (ε) is regarded as 1.0 in
129 channels.

130

131 Table. 1 Conservation equation.

Description	Conservation Equation	Computational domains
Mass	$\frac{\partial(\varepsilon\rho)}{\partial t} + \nabla\cdot(\varepsilon\rho v) = S_{\mathrm{m}}$	Channels, Porous electrodes
Momentum	$\frac{\partial}{\partial t}(\varepsilon\rho v) + \nabla\cdot(\varepsilon\rho vv) = -\varepsilon\nabla p + \nabla\cdot\left[\varepsilon\mu\left(\nabla v + (\nabla v)^{\mathrm{T}}\right)\right] + S_{\mathrm{u}}$	Channels, Porous electrodes
Species	$\frac{\partial}{\partial t}(\varepsilon\rho y_{\mathrm{i}}) + \nabla\cdot\left(-\rho y_{\mathrm{i}}\sum_{\mathrm{j}\neq\mathrm{i}}^{\mathrm{n}} D_{\mathrm{eff,ij}}\nabla x_{\mathrm{j}} + \rho v y_{\mathrm{i}}\right) = S_{\mathrm{i}}$	Channels, Porous electrodes
Energy	$\frac{\partial}{\partial t}(\varepsilon\rho c_{\mathrm{p}}T) + \nabla\cdot(\varepsilon\rho c_{\mathrm{p}} vT) = \nabla\cdot(\kappa_{\mathrm{eff}}\nabla T) + S_{\mathrm{T}}$	All domains

Electronic charge	$0 = \nabla \cdot \left(\sigma_{\text{ele}}^{\text{eff}} \nabla \varphi_{\text{ele}}\right) + S_{\text{ele}}$	Interconnects, Porous electrodes
Ionic charge	$0 = \nabla \cdot \left(\sigma_{\text{ion}}^{\text{eff}} \nabla \phi_{\text{ion}}\right) + S_{\text{ion}}$	ACL/CCL, Electrolyte

132

133 Table. 2 Source terms.

Source terms	Unit
$S_{\text{m}} = \begin{cases} 0 & \text{Channels} \\ S_{\text{CH}_4} + S_{\text{H}_2} + S_{\text{CO}} + S_{\text{H}_2\text{O}} + S_{\text{CO}_2} & \text{porous cathode} \\ S_{\text{O}_2} & \text{ACL} \end{cases}$	kg m^{-3} s^{-1}
$S_{\text{CH}_4} = -R_{\text{MSR}} M_{\text{CH}_4}$ cathode electrode	kg m^{-3} s^{-1}
$S_{\text{H}_2} = \begin{cases} \left(3R_{\text{MSR}} + R_{\text{WGSR}}\right) M_{\text{H}_2} & \text{CDL} \\ \dfrac{J_{\text{c}}}{2F} M_{\text{H}_2} + \left(3R_{\text{MSR}} + R_{\text{WGSR}}\right) M_{\text{H}_2} & \text{CCL} \end{cases}$	kg m^{-3} s^{-1}
$S_{\text{CO}} = \begin{cases} \left(R_{\text{MSR}} - R_{\text{WGSR}}\right) M_{\text{CO}} & \text{CDL} \\ \dfrac{J_{\text{c}}}{2F} M_{\text{CO}} + \left(R_{\text{MSR}} - R_{\text{WGSR}}\right) M_{\text{CO}} & \text{CCL} \end{cases}$	kg m^{-3} s^{-1}
$S_{\text{H}_2\text{O}} = \begin{cases} \left(-R_{\text{MSR}} - R_{\text{WGSR}}\right) M_{\text{H}_2\text{O}} & \text{CDL} \\ -\dfrac{J_{\text{c}}}{2F} M_{\text{H}_2\text{O}} - \left(R_{\text{MSR}} + R_{\text{WGSR}}\right) M_{\text{H}_2\text{O}} & \text{CCL} \end{cases}$	kg m^{-3} s^{-1}
$S_{\text{CO}_2} = \begin{cases} R_{\text{WGSR}} M_{\text{CO}_2} & \text{CDL} \\ -\dfrac{J_{\text{c}}}{2F} M_{\text{CO}_2} + R_{\text{WGSR}} M_{\text{CO}_2} & \text{CCL} \end{cases}$	kg m^{-3} s^{-1}
$S_{\text{O}_2} = \dfrac{J_{\text{a}}}{2F} M_{\text{O}_2}$ ACL	kg m^{-3} s^{-1}
$S_{\text{u}} = \begin{cases} 0 & \text{Channels} \\ -\dfrac{\mu}{K} \varepsilon^2 v & \text{porous electrodes} \end{cases}$	kg m^{-2} s^{-2}
$S_{\text{ohm}}^{\text{ele}} = \left\|\nabla \varphi_{\text{ele}}\right\| \kappa_{\text{ele}}^{\text{eff}}$	W m^{-3}
$S_{\text{ohm}}^{\text{ion}} = \left\|\nabla \varphi_{\text{ion}}\right\| \kappa_{\text{ion}}^{\text{eff}}$	W m^{-3}

$$S_{\mathrm{rev}}=\begin{cases}J_{\mathrm{a}}\dfrac{\Delta S_{\mathrm{a}}T}{4F} & \text{anode}\\ J_{\mathrm{c}}\dfrac{\Delta S_{\mathrm{c}}T}{2F} & \text{cathode}\end{cases} \quad \mathrm{W\ m^{-3}}$$

$$S_{\mathrm{irr}}=\begin{cases}J_{\mathrm{a}}\left|\eta_{\mathrm{act}}^{\mathrm{a}}\right| & \text{anode}\\ J_{\mathrm{c}}\left|\eta_{\mathrm{act}}^{\mathrm{c}}\right| & \text{cathode}\end{cases} \quad \mathrm{W\ m^{-3}}$$

$$S_{\mathrm{che}}=R_{\mathrm{MSR}}H_{\mathrm{MSR}}+R_{\mathrm{WGSR}}H_{\mathrm{WGSR}} \quad \mathrm{W\ m^{-3}}$$

$$S_{\mathrm{T}}=\begin{cases}0 & \text{Channels}\\ S_{\mathrm{ohm}} & \text{Interconnects, ADL, Electrolyte}\\ S_{\mathrm{ohm}}+S_{\mathrm{che}} & \text{CDL}\\ S_{\mathrm{ohm}}^{\mathrm{ele}}+S_{\mathrm{ohm}}^{\mathrm{ion}}+S_{\mathrm{rev}}+S_{\mathrm{irr}} & \text{ACL}\\ S_{\mathrm{ohm}}^{\mathrm{ele}}+S_{\mathrm{ohm}}^{\mathrm{ion}}+S_{\mathrm{rev}}+S_{\mathrm{irr}}+S_{\mathrm{che}} & \text{CCL}\end{cases} \quad \mathrm{W\ m^{-3}}$$

$$S_{\mathrm{ele}}=\begin{cases}J_{\mathrm{c}} & \text{CLC}\\ -J_{\mathrm{a}} & \text{CLA}\end{cases} \quad \mathrm{A\ m^{-3}}$$

$$S_{\mathrm{ion}}=\begin{cases}-J_{\mathrm{c}} & \text{CLC}\\ J_{\mathrm{a}} & \text{CLA}\end{cases} \quad \mathrm{A\ m^{-3}}$$

2.2 Multi-component diffusion process

The gas diffusion in the porous electrodes is mainly by two mechanisms: Knudsen diffusion and molecular diffusion [32]. The Knudsen diffusion represents the collisions between the gas molecules and pore walls [33]. Moreover, a variety of gas components is involved in the chemical and electrochemical reactions, and the molecular diffusion refers to the collisions among these gas molecules. The expressions for Knudsen diffusion coefficient and binary diffusion coefficient, $D_{k,\mathrm{ij}}$ and D_{ij}, as well as the effective diffusion coefficient ($D_{\mathrm{eff,ij}}$) in the species conservation equation are given in Table 3 [34-36].

Table. 3 Multi-component diffusion coefficients.

Diffusion coefficient	Equation

Knudsen diffusion coefficient [34]

$$D_{\mathrm{k,ij}} = \frac{2}{3} r \sqrt{\frac{8RT}{\pi M_{\mathrm{ij}}}}$$

Binary diffusion coefficient [35]

$$D_{\mathrm{ij}} = \frac{0.0101 T^{1.75}}{p M_{\mathrm{ij}}^{1/2} \left[V_{\mathrm{i}}^{1/3} + V_{\mathrm{k}}^{1/3} \right]^2}$$

Effective diffusion coefficient [36]

$$D_{\mathrm{eff,ij}} = \begin{cases} \dfrac{1 - x_{\mathrm{j}}}{\sum_{\mathrm{j} \neq \mathrm{i}} \dfrac{x_{\mathrm{j}}}{D_{\mathrm{ij}}}} & \text{channels} \\ \dfrac{\varepsilon}{\tau} \left(\dfrac{1}{\dfrac{\sum_{\mathrm{j} \neq \mathrm{i}} \dfrac{x_{\mathrm{j}}}{D_{\mathrm{ij}}}}{1 - x_{\mathrm{j}}} + \dfrac{1}{D_{\mathrm{k,ij}}}} \right) & \text{porous electrodes} \end{cases}$$

2.3 Electrochemical model

The source terms of charge conservation equations, which represent the current densities caused by electrochemical reactions, are derived from Butler-Volmer equations:

$$J_{\mathrm{c}} = \left(j_{0,\mathrm{c}}^{\mathrm{H_2O}} + j_{0,\mathrm{c}}^{\mathrm{CO_2}} \right) \left(\exp\left(\alpha \frac{n_{\mathrm{e}} F}{RT} \eta_{\mathrm{act}} \right) - \exp\left(-(1-\alpha) \frac{n_{\mathrm{e}} F}{RT} \eta_{\mathrm{act}} \right) \right) \tag{6}$$

$$J_{\mathrm{a}} = j_{0,\mathrm{a}} \left(\exp\left(\beta \frac{n_{\mathrm{e}} F}{RT} \eta_{\mathrm{act}} \right) - \exp\left(-(1-\beta) \frac{n_{\mathrm{e}} F}{RT} \eta_{\mathrm{act}} \right) \right) \tag{7}$$

where α, β are the charge transfer coefficients, η_{act} (V) the activation overpotential, $j_{0,\mathrm{a}}$ and $j_{0,\mathrm{c}}$ (A m^{-3}) the exchange current density, which can be expressed as:

$$j_{0,\mathrm{c}}^{\mathrm{H_2O}} = \frac{\gamma_{\mathrm{c,H_2O}} RT}{n_{\mathrm{e}} F} \left(\frac{p_{\mathrm{H_2O}}}{p_{\mathrm{ref,H_2O}}} \right)^{\mathrm{m}} \exp\left(-\frac{E_{\mathrm{act,c}}}{RT} \right) \tag{8}$$

$$j_{0,\mathrm{c}}^{\mathrm{CO_2}} = \frac{\gamma_{\mathrm{c,CO_2}} RT}{n_{\mathrm{e}} F} \left(\frac{p_{\mathrm{CO_2}}}{p_{\mathrm{ref,CO_2}}} \right)^{\mathrm{n}} \exp\left(-\frac{E_{\mathrm{act,c}}}{RT} \right) \tag{9}$$

$$j_{0,a} = \frac{\gamma_a RT}{n_e F}\left(\frac{p_{O_2}}{p_{ref,O_2}}\right)^k \exp\left(-\frac{E_{act,a}}{RT}\right) \quad (10)$$

where γ_a and γ_c are the adjustable parameters which are used to fit the experiment results. E_{act} (J mol^{-1}) is the activation energy. In addition, the effective electron and ion conductivity in electronic/ionic charge conservation equations, σ^{eff} (S m^{-1}), is determined by following expressions:

$$\sigma_{ele}^{eff} = \omega\left(\frac{1-\varepsilon}{\tau}\right)\sigma_{ele}^{0} \quad (11)$$

$$\sigma_{ion}^{eff} = (1-\omega)\left(\frac{1-\varepsilon}{\tau}\right)\sigma_{ion}^{0} \quad (12)$$

where ω is the volume fraction of electron conducting particles, τ the tortuosity, and σ^0 the conductivity of the pure electron/ion conducting particles.

2.4 Chemical model

In the porous cathode, the Ni particles not only act as the electron conductors but also function as catalyst for internal reforming reactions. Several internal reforming reactions occur in co-electrolysis process of H_2O and CO_2. The WGSR and MSR are considered in the present study. The Haberman's model [37] is widely used to calculate the reaction rates for the internal reforming reactions, and the relevant expressions are listed in Table 4. The forward rate constants (k_{rf}/k_{sf}) and the equilibrium constants (K_{pr}/K_{ps}) are correlation functions of temperature calculated by fitting experiment data, as shown in [36]. The forward MSR is a strong endothermic reaction while the forward WGSR is an exothermic reaction, and the reaction heats can be calculated as the expressions shown below.

Table. 4 Internal reforming reactions.

Parameters	Mathematical expressions	Unit
Reaction rates		
MSR	$R_{MSR} = k_{rf}\left(p_{CH_4}p_{H_2O} - \frac{p_{CO}\left(p_{H_2}\right)^3}{K_{pr}}\right)$	mol m^{-3} s^{-1}

WGSR	$R_{\mathrm{WGSR}} = k_{\mathrm{sf}}\left(p_{\mathrm{H_2O}} p_{\mathrm{CO}} - \frac{p_{\mathrm{H_2}} p_{\mathrm{CO_2}}}{K_{\mathrm{ps}}} \right)$	mol m^{-3} s^{-1}
Reaction heats		
MSR [36]	$H_{\mathrm{MSR}} = -\left(206205.5 + 19.5175T\right)$	J mol^{-1}
WGSR [36]	$H_{\mathrm{WGSR}} = 45063 - 10.28T$	J mol^{-1}

2.5 Cell electrolysis efficiency

During the co-electrolysis process of H_2O and CO_2, the electricity input is converted into chemical energy of products. The cell electrolysis efficiency is normally defined as the ratio of the total lower heat value (LHV) of products and power consumption [38]:

$$\eta_{\mathrm{SOEC}} = \frac{\sum_{\mathrm{i=H_2,CO,CH_4}} \left(\left(n_{\mathrm{i,out}} - n_{\mathrm{i,in}} \right) \times LHV_{\mathrm{i}} \right)}{E_{\mathrm{input}}} \tag{13}$$

where n_{i} (mol s^{-1}) is the flow flux of specie i. E_{input} the electrical power consumption by co-electrolysis, which can be simply calculated by multiplying the voltage demand for electrolysis (V_{demand}) and operating current:

$$E_{\mathrm{input}} = V_{\mathrm{demand}} \cdot J \tag{14}$$

2.6 Boundary conditions

For all cases, the electrolysis cell operates in galvanostatic mode, and the mass flow rates are implemented in anode and cathode inlets at different operating current densities:

$$m_{\mathrm{a}} = \sum_{1}^{i} \left(x_{\mathrm{i}} M_{\mathrm{i}} \right) \cdot \frac{J A_{\mathrm{act}} \delta_{\mathrm{ACL}}}{4 F x_{\mathrm{O_2}}} \cdot \xi \tag{15}$$

$$m_{\mathrm{c}} = \sum_{1}^{i} \left(x_{\mathrm{i}} M_{\mathrm{i}} \right) \cdot \frac{J A_{\mathrm{act}} \delta_{\mathrm{CCL}}}{\left(2 F x_{\mathrm{H_2O}} + 2 F x_{\mathrm{CO_2}} + 2 F x_{\mathrm{CH_4}} \right) \mu_{\mathrm{f}}} \tag{16}$$

where A_{act} (m^2) is the cell active area, δ_{ACL} and δ_{CCL} (m) the thickness of ACL and CCL, respectively, ξ the air stoichiometric ratio, u_f the gas utilization of cathode. The boundary conditions and settings are listed in Table 5. When there is no physical flux through the surface, the boundary condition is noted as "Insulation" in Table 5. For electronic and ionic potential conservation, it should be mentioned that the operating current density (galvanostatic mode) or total overpotential (constant voltage mode) is specified at anode terminal surface, while a reference electronic potential is set to be 0 V at cathode terminal surface [39]. The total overpotential (η_{tot}) can be calculated by extracting the reversible voltage from the voltage demand for co-electrolysis:

$$\eta_{tot} = V_{demand} - E_{rev} \tag{17}$$

$$E_{rev} = \frac{1}{x_{H_2O} + x_{CO_2}} \left(x_{H_2O} E_{rev,H_2} + x_{CO_2} E_{rev,CO} \right) \tag{18}$$

where E_{rev} is the reversible voltage, which can be calculated by the Nernst equation (Eqn. 19,20).

$$E_{rev,H_2} = 1.2535 - 0.000229772T + \frac{RT}{nF} \ln \frac{p_{H_2} p_{O_2}^{0.5} p_0^{-0.5}}{p_{H_2O}} \tag{19}$$

$$E_{rev,CO} = 1.466 - 0.0004476T + \frac{RT}{nF} \ln \frac{p_{CO} p_{O_2}^{0.5} p_0^{-0.5}}{p_{CO_2}} \tag{20}$$

It should be mentioned that the partial pressures used in Eqn. 19 and 20 are derived from the interface of catalyst layer and electrolyte, thus changes of reversible voltage imply the value of the concentration overpotential [36]. The relevant cell parameters of above equations and cell operation conditions are listed in Table 6 [40-43], and the physical properties of solid parts are shown in Table 7 [43,44].

Table. 5 Boundary conditions or settings for the SOEC model in Fluent.

Boundary/interface	Gas flow	Mass transport	Heat transport	Electronic field
Gas inlet	Laminar flow	Mass flow	Operating temperature	

Gas outlet	Pressure	Convective flux	Convective flux	
Channel/electrode	Continuous	Insulation	Continuous	Insulation
Interconnect/channel	No slip	Insulation	Continuous	Insulation
Interconnect/electrode	Insulation	Insulation	Continuous	Continuous
Electrolyte/electrode	Insulation	Insulation	Continuous	Insulation
Anode terminal surface	Insulation	Insulation	Adiabatic	Electric potential
Cathode terminal surface	Insulation	Insulation	Adiabatic	Electric potential
Other external walls	Insulation	Insulation	Adiabatic	Insulation

204

205 Table. 6 Model parameters and operating conditions.

Parameters	Value
Electrochemistry parameters	
Transfer coefficient in anode/cathode [40]	0.5/0.5
Activation energy of anode (J mol^{-1}) [41]	120,000
Activation energy of cathode (J mol^{-1}) [41]	120,000
Porosity	0.36
Tortuosity [24]	3.0
Volume fraction of electron-conducting Particles [42]	0.5
Adjustable parameters	
$\gamma_{c,H2O}$, $\gamma_{c,CO2}$, γ_a	8.2×10^{14}, 3.28×10^{14}, 2.95×10^{14}
Exponent for exchange current density	
m, n, k	0.5, 0.5, 0.25
Anode electric conductivity (S m^{-1}) [43]	$\frac{4.2\times10^{7}}{T}\exp\left(\frac{-1200}{T}\right)$
Cathode electric conductivity (S m^{-1}) [43]	$\frac{9.5\times10^{7}}{T}\exp\left(\frac{-1150}{T}\right)$
Electrolyte ionic conductivity (S m^{-1}) [43]	$33.4\times10^{3}\exp\left(\frac{-10300}{T}\right)$
Operating conditions at base case	
Operating pressure (atm)	1.0
Operating temperature (K)	1073
Cathode gas utilization	0.5
Air stoichiometric ratio	2.0
Flow arrangement	Counter-flow
Gas composition	

Cathode	45 vol% H_2O, 45 vol% CO_2, 10 vol% H_2,
Anode	Air (21% O_2, 79% N_2)

206

207 Table. 7 Physical properties of the solid parts.

Parameters	Anode	Electrolyte	Cathode	Interconnect
Thermal conductivity (W m^{-1} K^{-1}) [44]	6.0	2.7	11.0	20.0
Density (kg m^{-3}) [43]	3030	5160	3310	3030
Specific heat capacity (J kg^{-1} K^{-1}) [43]	430	470	450	550

208

209 *2.7 Numerical procedures*

210 The numerical simulation for co-electrolysis of SOEC is conducted with the commercial
211 software Fluent. The internal reforming reactions, multi-component diffusion process and
212 electrochemical process (electronic and ionic charge conservation) are considered, and the
213 related equations are implemented with the user defined functions (UDF) in Fluent. In order
214 to handle the coupling between pressure and velocity, the SIMPLE algorithm is applied in this
215 model. Besides, the second order upwind scheme is used to calculate the convective terms.
216 The residual criteria of all equations are set as 1.0×10^{-9}. When the values of residual curves
217 are less than the residual criteria and the residual curves level off, the iteration is considered to
218 reach convergence.

219 The grid sensitivity analysis was performed by increasing the number of grids in different
220 directions. The numbers of grids are changing from 5 to 10, 8 to 16, 10 to 20 and 190 to 220
221 for channel width ($W_{channel}$), channel height ($H_{channel}$), PEN layers (δ) and cell length (L_{cell}),
222 respectively. The voltage and total heat transfer rates of outlet are checked. The changes are
223 below 0.02%, which can be neglected. The number of final mesh grids is 3,752,100 for Type
224 A, and the criteria for the final grid density are listed in Table 8.

225

226 Table. 8 Cell geometry and grid numbers.

Parameters	Value	Grid numbers
Cell length (L_{cell}, mm)	50	190
Cell width (W_{cell}, mm)	50	255
Channel width ($W_{channel}$, mm)	1	5
Channel height ($H_{channel}$, mm)	1	8
Rib width (W_{rib}, mm)	1	5
Interconnect width (W_{inter}, mm)	0.5	5
Interconnect height (H_{inter}, mm)	1.5	13
Porous material length (L_{porous}, mm)	50	190
Porous material width (W_{porous}, mm)	50	255
Porous material height (H_{porous}, mm)	1	8
Distribution area width (W_{dis}, mm)	2.5	10
ADL thickness (δ_{ADL}, μm)	30	10
CDL thickness (δ_{CDL}, μm)	300	10
ACL thickness (δ_{ACL}, μm)	15	10
CCL thickness (δ_{CCL}, μm)	10	10
Electrolyte thickness (δ_{ELE}, μm)	10	10

2.8 Model verification

The model described above has been compared with experimental results carefully in our previous research [45]. And the polarization curves derived by simulation results are fitted while keeping the operating condition and electrode structure consistent with the experiment. Three sets of working parameters (operating temperature, cathode composition and operating pressure) are compared, and the results show a good agreement.

3. Results and discussion

3.1 Effects of flow field designs

In this section, four types of flow field designs (shown in Fig. 2a) are compared and evaluated in term of the thermal-fluid-electrical distributions. Three typical traditional flow fields are selected: parallel, serpentine and parallel serpentine (Type A, B and C). The cell dimension is fixed as 50mm both for width and length. Each flow field has five entries. The width of ribs between channels, ribs connected to surroundings and channels are the same for three kinds of flow fields, and the value of these are 1.0, 0.5 and 1.0 mm, respectively. The cell geometry parameters are listed in Table 8. In addition, the rib-channel structure is replaced by porous material to fabricate the porous flow field (Type D). In other words, the areas occupied by channel and rib are all changed to porous material for Type D. The comparison of geometric structure between traditional flow fields and porous material flow field is also shown in Fig. 2b.

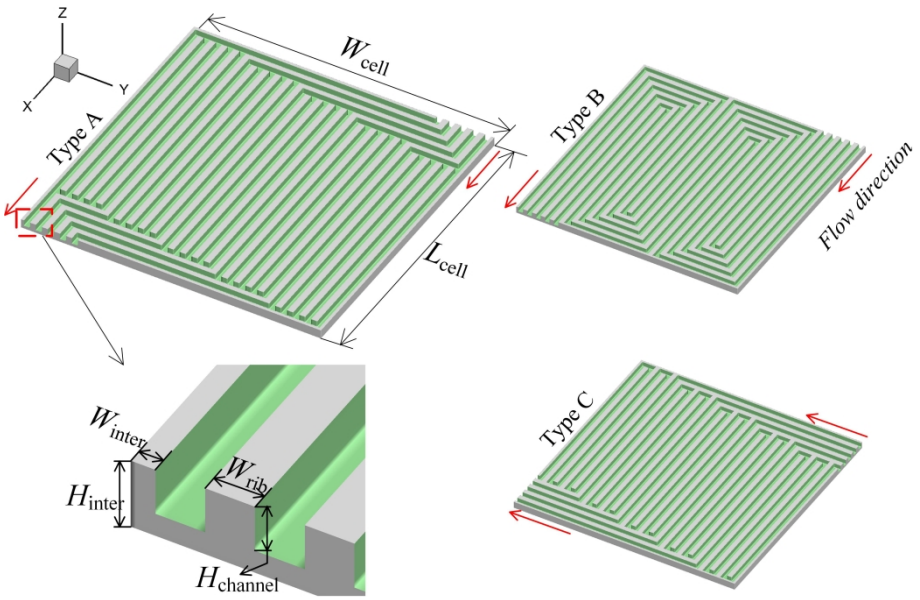

(a)

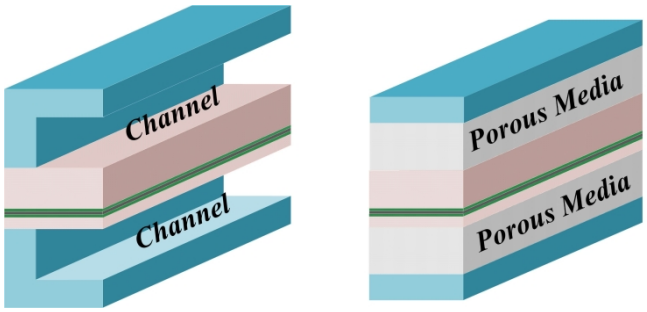

(b)

Fig. 2 (a) Geometries of three kinds of traditional flow fields, (b) Comparison of traditional flow field and porous flow field.

3.1.1 Cell performance

Fig. 3 shows the polarization curves and electrolysis efficiency of four designs. The results indicate the differences between Type A, Type B and Type C are not significant. The related curves are nearly equal under various operating current densities for Type A and Type C. For Type B, the voltage demand only decreases 0.012 V at high current density (2.5 A cm^{-2}), while the electrolysis efficiency increases 0.4%, compared to that of Type A. For rib-channel structure, with decreasing ratio of rib width to channel width, the gas is much easier to diffuse into the porous electrode, especially in comparatively thin anode (10-100 μm). Meanwhile, the cell conductivity is decreased with decreasing rib width. In contrast, the larger ratio may cause the lack of gas in the porous electrode region under the ribs, which will result in degraded performance. Thus, this ratio has a remarkable impact on species and electron transport. Ideally, the flow field design needs to improve the capability of gas diffusion and simultaneously ensure sufficient electronic conductivity. The flow field design requirements can be satisfied by utilizing porous material. This flow field is easily fabricated, and the material can be porous cermet or metal foam (e.g. Cu-Mn Foam [29]). The results shown in Fig. 3 indicate that the porous media flow field (Type D) has a better effect on reducing the voltage demand and increasing electrolysis efficiency. The voltage demand decreases by 0.026V at 2.5 A cm^{-2}, while the electrolysis efficiency increases by 4.78%. The performance improvement mainly comes from the increase of conductivity and more uniform species

distribution. It should be noted that, in Section 3.2, the structure optimization of porous material flow field is performed, and the comparisons among traditional, initial and optimized flow fields with respect to species distribution are displayed in related figures.

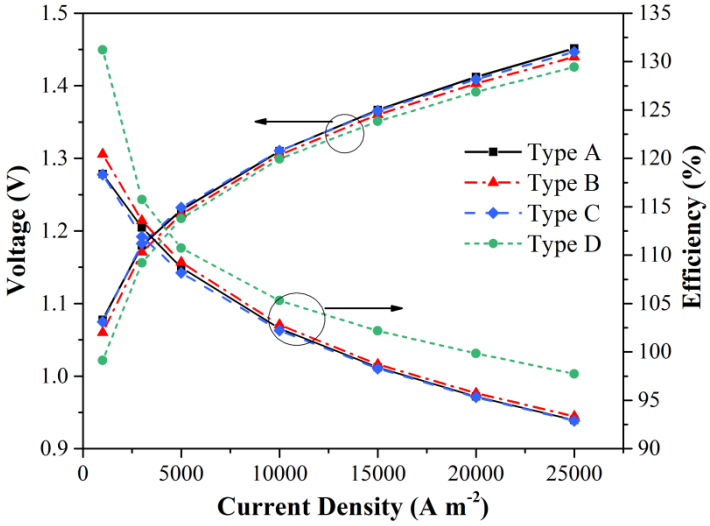

Fig. 3 C-V-E curves of the co-electrolysis SOEC with various flow fields.

3.1.2 Pressure and velocity distribution

The main role of the excessive air in anode channel is to realize good thermal management. Consequently, air flux is generally larger than the stoichiometrically needed amount, which results in a large anode pressure drop. Fig. 4a depicts the pressure field inside anode channel. Note that the gauge pressures are adopted in this figure. The highest pressure drop is found in Type D, followed by Type B and C, and lowest in Type A, for the dominant factor that affects pressure distributions of traditional flow fields is the single channel length. The SOFC adopting serpentine flow field can present a better performance at the cost of larger pressure drop. Thus, for large scale applications, the entries of serpentine flow field should be added in order to avoid the too large pressure drop and structural stress. In addition, it is noteworthy that the pressure drop of Type D outclass that of other types of flow fields due to the porous structure. The existing structure still needs to be improved to reduce the pressure drop, and the optimized designs are discussed in Section 3.2. Fig. 4b compares the velocity contours of

Type A and Type D. It can be observed that the maximum velocity is around the corner, and the maximum velocity of Type A is larger than Type D. Dong et al. [18] adopted a manifold with multi-stage channel to achieve a good flow uniformity, which indicates that the multi-channel geometry can effectively make the flow field uniform. Similarly, the multi-channel parallel flow field of Type A can offer uniform velocity distribution in each different single channel.

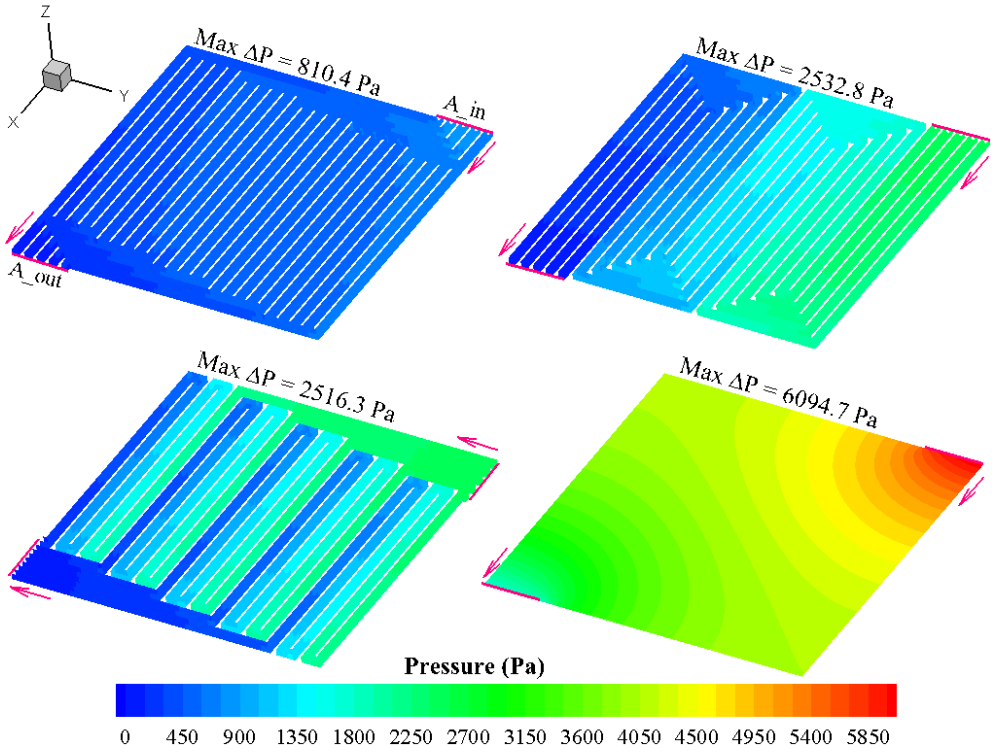

(a)

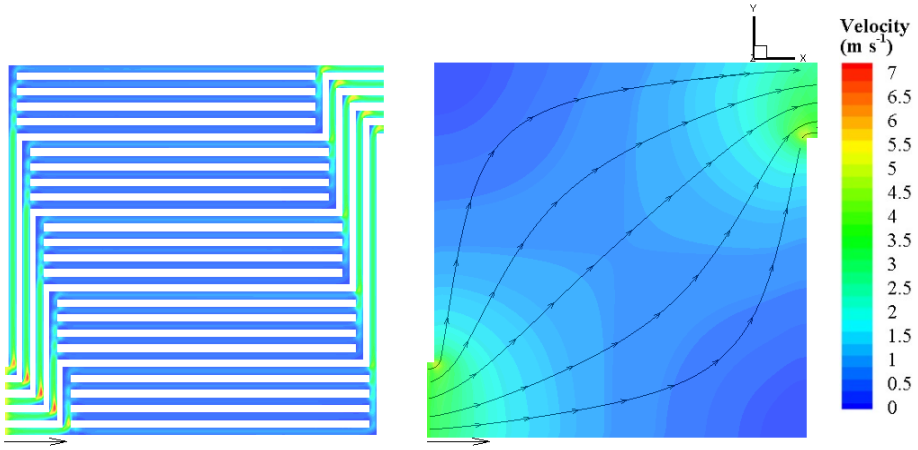

(b)

Fig. 4 (a) Pressure distribution for four kinds of flow fields, (b) Velocity in cathode channel.

3.1.3 Temperature distribution and thermal analysis

Since the required voltages in the base case (1.5 A cm^{-2}) are slightly higher than the thermal neutral voltages (TNV) for the co-electrolysis, the heat generated in cell exceeds the heat demand for electrochemical reactions. As shown in Fig. 5, the heat accumulates along the air flow direction, which increases the cell temperature. Meanwhile, due to the counter-flow configuration, the highest temperature area appears in the middle of the cell. For traditional flow fields, although their maximum temperature drops are very close, it can be clearly seen from the figure that the high-temperature region of Type B is the largest, followed by Type A, and Type C. The parallel flow fields have a better heat transfer capability due to its short single channel length and low flow velocity. On the contrary, the single channel length of serpentine flow field is the longest, which leads to large flow velocity and heat accumulation. For parallel serpentine flow field, the heat transfer between the adjacent flow channels of different entries is strong, and it can reduce the temperature of the electrolysis cell to some extent.

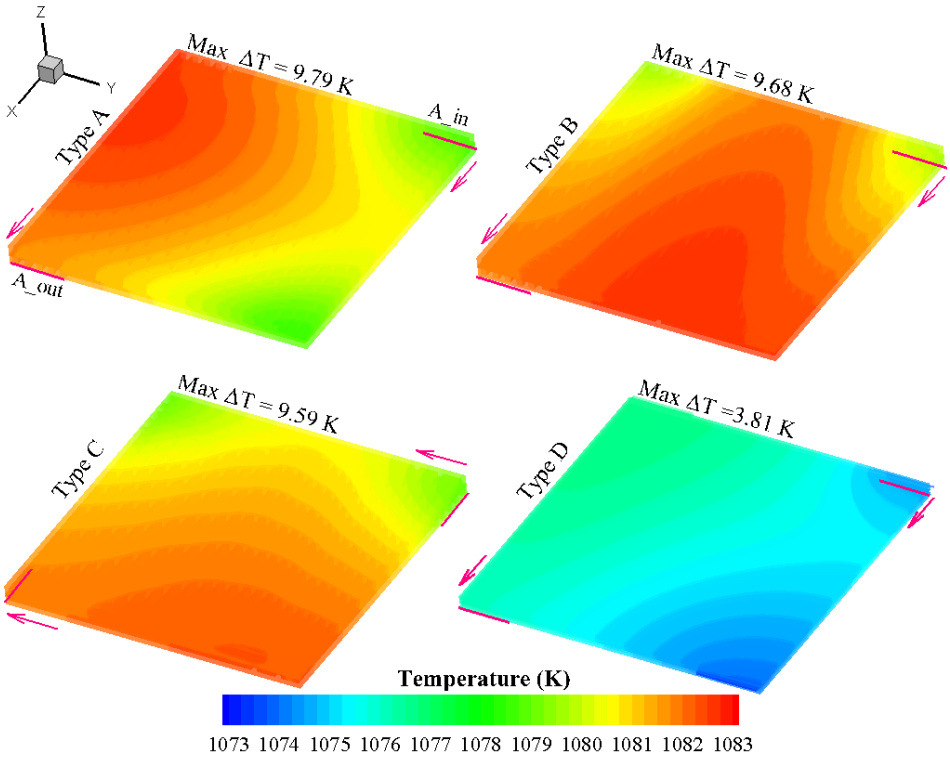

Fig. 5 Temperature distribution for four kinds of flow fields.

Moreover, for porous media flow field (Type D), the overall temperature and maximum temperature difference (3.81K) are much lower than that in traditional flow fields (about 9.5K). In order to elucidate the temperature influence factors for porous media flow field, the thermal analysis is conducted by evaluating the heat source terms of Type A and Type D in Table 9. The differences of total heat generation between Type D and other types are mainly in ohmic and irreversible heat. On the one hand, the porous material is fully contact with interconnect and electrode, which enhances the cell conductivity and reduces the ohmic resistance. On the other hand, the irreversible heat is related to the activation overpotential. The lower overall temperature hinders the transport of oxygen ions, and this results in the increase of activation overpotential. Under the combined action of these two aspects, the total heat generation of Type D is smaller than other three kinds of flow fields. The maximum temperature difference will get large with the increasing of current. Besides, conscious choice of operating mode (exothermic, endothermic or thermal neutral) according to practical needs has great impact on reaching optimal efficiency for SOEC system [46]. So when SOEC needs to operate in a high current mode, the novel porous material can effectively reduce the influence of thermal stress.

Table. 9 Heat source terms (Unit W).

	Ohm	Rev (anode)	Rev (cathode)	Irr	Che	Total
Type A	6.137	13.000	-26.652	9.685	-1.151	1.019
Type D	5.295	12.933	-26.493	10.246	-1.255	0.726

3.1.4 Chemical reaction distribution

In Fig. 6, the internal reforming reactions rates of Type A and Type D are shown and compared in three vertical slices of porous cathode layer. Overall, for both WGSR (Fig. 6a) and MSR (Fig. 6b), the reverse reactions are dominant due to the high operating temperature and inlet gas components. The reverse WGSR rates decrease along the flow direction for two types of flow fields. And in the vertical direction, the reverse WGSR rates get lower when closing to the electrolyte. This is because that H_2O is easier to diffuse than CO_2 in porous

layer. Unlike WGSR, the MSR rates are close to zero in most areas. And the difference of reaction rates is not obvious in the vertical direction. As shown in Fig. 6a, the reverse WGSR rates under channels are significantly larger than that under ribs, and it is mainly caused by the difference between the relative concentration of CO_2 and H_2O in these regions. For Type D, there is a saltation of chemical reaction in the downstream region on both sides of the diagonal line. But in general, the chemical reaction distribution of porous material flow field is more uniform compared with traditional flow field, which is conductive to the uniform distribution of species.

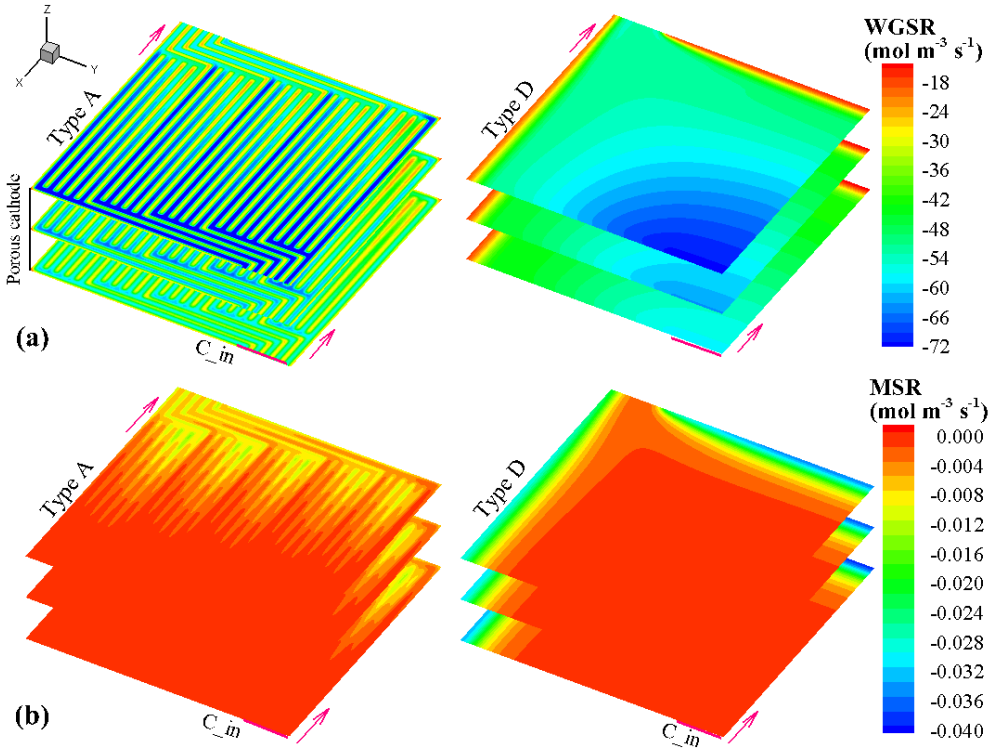

Fig. 6 Internal reforming reaction rates distribution (a) WGSR rates, (b) MSR rates.

3.1.5 Electrolysis rates distribution

The electrolysis rates are related to the microstructural parameters, species concentration and flow field structure. The non-uniform distribution of electrolysis rates will lead to negative outcomes, such as high ohmic loss, large temperature gradient and poor performance. For co-electrolysis process inside SOEC, the electrolysis reactions of H_2O and CO_2 occur in parallel and relatively independent way, thus they are discussed separately in Fig. 7.

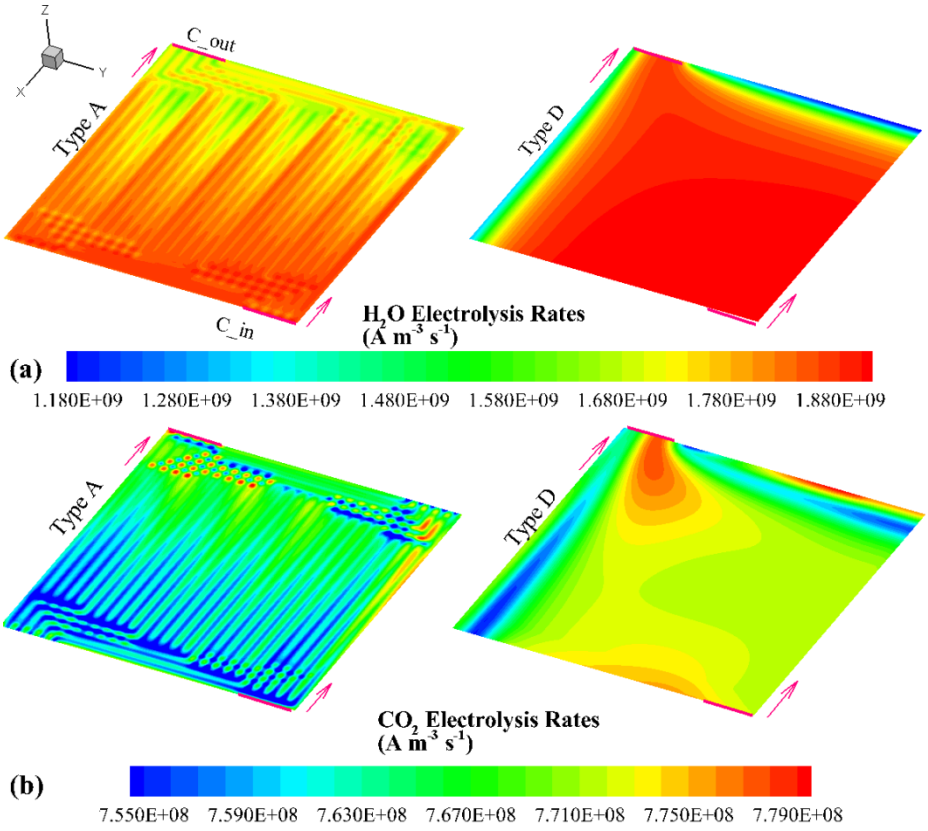

Fig. 7 Electrochemical reaction rates distribution (a) H_2O electrolysis rates, (b) CO_2 electrolysis rates.

Fig. 7a and Fig. 7b show the electrolysis rates distributions of H_2O and CO_2 at the interface of catalyst layer and electrolyte, respectively. As can be shown in Fig. 7a, for traditional straight channel (Type A), the electrolysis rates distribution of H_2O manifests a geometrically similar characteristic. But the counter-flow configuration can result in a checkerboard distribution in some areas. The electrolysis rates distribution of CO_2 is mainly affected by WGSR rates. The reverse WGSR consumes H_2O to produce CO_2, which supplements the CO_2 in the catalytic layer to a large extent. Therefore, the electrolysis rates distribution of CO_2 is opposite to that of H_2O, and it gradually increases along the gas channel. Compared to Type A, the electrolysis rates of Type D distribute much evenly due to the uniform porous media structure. But the low H_2O concentration leads to low electrolysis rates in edge areas. As mentioned above, the non-uniform distribution beside edges is harmful to cell performance, and this

problem can be resolved by increasing the distribution uniformity of species concentration. To address the non-uniform species concentration distribution in detail, the porous flow field is further optimized in following section.

3.2 Porous media flow field optimization

Compared with the traditional flow fields, the porous media flow fields have larger diffusion resistance, which may cause insufficient downstream gas concentration when the relative flow distance is long. Therefore, it is very important to reasonably optimize the structures of the inlet/outlet distribution areas to improve the performance of the electrolysis cell. For this reason, four kinds of porous media flow fields are designed and shown in the Fig. 8. The distribution areas are noted in Fig. 8 as the deep grey areas. They are open channels, and the role of these areas is to distribute the gas, and the gas will go into them first to achieve a uniform distribution. The difference between them lies in the number of inlets and whether there are distribution zones for the inlets and outlets. Type D and Type F have one inlet outlet, when Type E and Type F have two inlets and outlets.

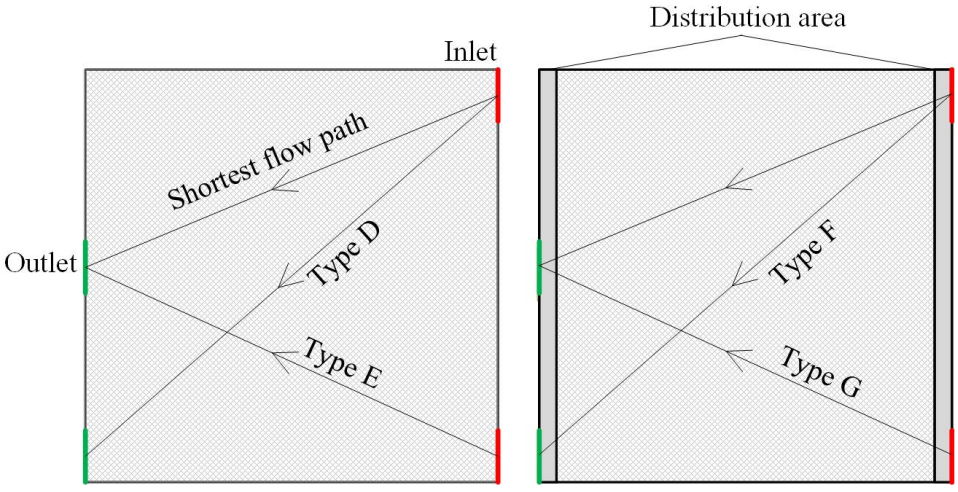

Fig. 8 The geometries of four types of porous material flow fields.

Fig. 9 shows the polarization curves of four porous media flow fields, and it can be found that the fourth design has a better performance when the operating current density is larger than

0.5 A cm^{-2}. At 2.5 A cm^{-2}， the voltage demand of Type G is 0.062 V less than that of Type A. The main reason is that the gas distribution in the cell with multiple inlets and distribution zones is more uniform, as shown in Fig. 10. By the same token, the uniform gas concentration contributes to the electrochemical reactions under lower current density (less tan 0.5 A cm^{-2}). But in this case, the overall co-electrolysis is endothermic, which results in the increase of voltage demand. It should be noted that the concentration distribution of CO_2 is not shown because it is similar to that of H_2O.

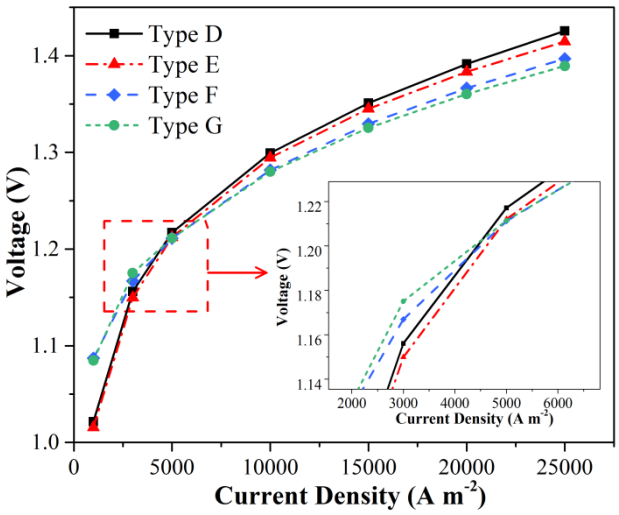

Fig. 9 C-V curves of SOEC with four kinds of porous material flow fields.

For one inlet design (Fig. 10a), the H_2O concentration is highest at the inlet and decreases along the diagonal. In the downstream region on both sides of the diagonal line, the low H_2O concentration is due to deviation from the main flow direction and the influence of the reverse WGSR. Compared with one inlet, the flow field with two inlets has a smaller low gas concentration area, but the concentration on both sides of the outlet remains low. In order to further optimize the porous material flow field, the distribution zones are added at the inlet and outlet sides. By comparing the difference of component distribution, the optimized flow fields (Type G) can increase the distribution uniformity and significantly improve the lowest H_2O concentration in the downstream area. In addition, the optimum flow field can completely eliminate the gas lacked area which appears in traditional flow field (Type A), that

is, the restrictions on gas distribution in typical rib-channel structure can be broken with the optimized porous material flow field. Moreover, after optimization, the maximum pressure drops of Type F and Type G are 3740 Pa and 2420 Pa, respectively, which are much lower than that of Type D and Type E.

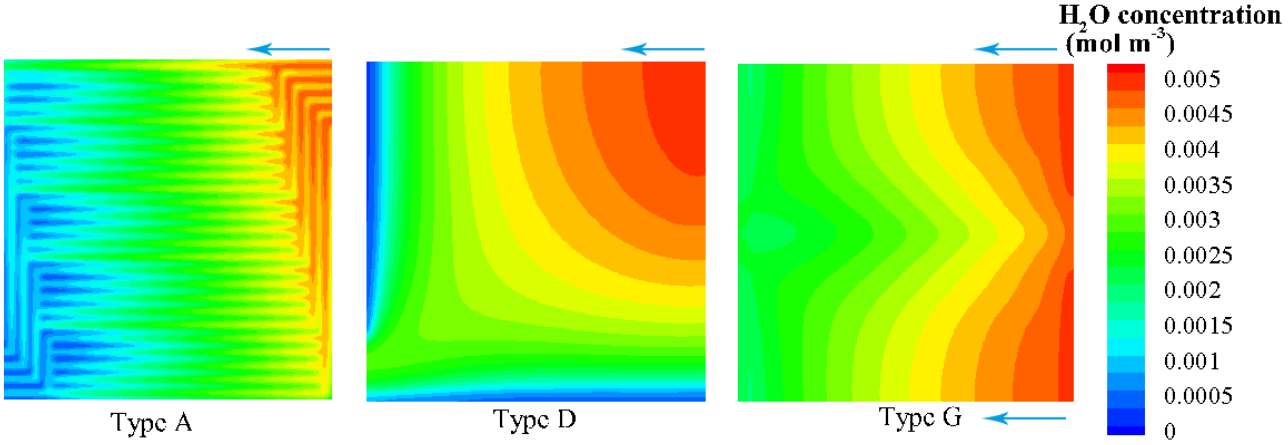

Fig. 10 H_2O concentration distribution at the interface of CDL and CCL.

3.3 Effects of porous material flow field configurations

The simulation results of Wei et al. [20] indicates that it is necessary to design distribution areas for the porous material flow field. In this section, the effects of porous material flow field configurations are investigated by comparing the C-V curves (Fig. 11). The anode configuration means that the porous material flow field is used in anode when the parallel flow field is used in cathode. Conversely, the cathode configuration adopts the parallel channel as anode flow field, and the porous material is used in cathode. Then the polarization curves of these two configurations and Type E are plotted in Fig. 11. As we can see, Type E, which adopts porous material flow field both sides, has the lowest electrolysis voltage demand, followed by anode configuration, and highest in cathode configuration. That is, the performance improvement of porous material flow field is more evident in anode. For typical cathode-supported SOEC, the anode porous layer is generally thin (30-100μm), which is much thinner than cathode support layer. This will cause the long transverse transfer of electrons, because these electrons have to first pass the joint of rib and electrode and then

transfer to the areas away from rib. And this process will increase the ohmic loss to some extent, which will decrease the cell performance.

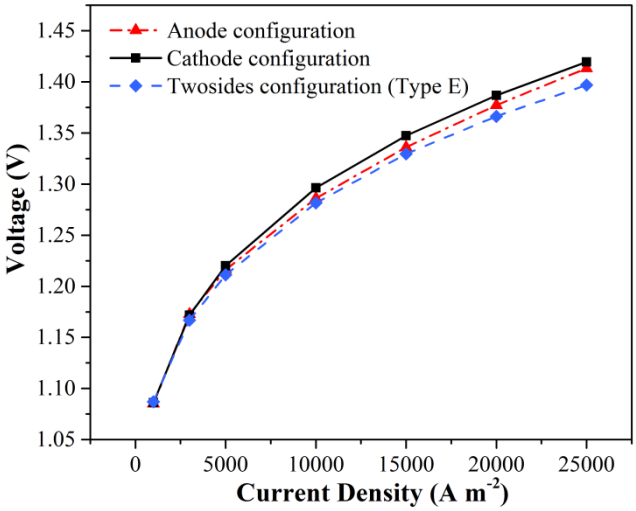

Fig. 11 C-V curves of SOEC with different porous material flow field configurations.

4. Conclusion

A comprehensive three-dimensional model is developed in this study to evaluate the SOEC performance when adopting various flow fields. And a novel porous material flow field design is proposed and compared with three types of traditional flow fields. It is found that the new type of porous material flow field can effectively improve the cell performance in the respect of reducing electrolysis voltage demand (0.026V at 2.5 A cm^{-2}) and increasing electrolysis efficiency (4.78% at 2.5 A cm^{-2}). In order to elucidate the mechanisms, the multi-physical fields are shown and analyzed in detail. The porous material flow field has advantages over traditional flow fields on species concentration, temperature and electrochemical reaction distribution. The fully contact structure can greatly enhance the conductivity and benefit the gas diffusion from channel to porous layer, which contributes to the decrease of ohmic heat and the uniform gas distribution inside porous layer. Because the operating voltage is a shade bigger than thermal neutral voltages, the cell operates in a slightly exothermic condition. The maximum temperature difference of the porous material flow field

is 3.81K at 1.5A cm^{-2}, which is significantly less than other types of flow fields. The thermal analysis is conducted by analyzing the values of heat source terms. It can be found that the novel flow field can effectively reduce the ohmic heat. Besides, the results show that the traditional flow fields are still subjected to the rib-channel structure, which will result in a nonuniform chemical and electrochemical distributions compared to porous material flow field. Then the porous material flow field is further optimized, and the gas lacked area appearing in parallel and unoptimized flow field can be fully eliminated. And the cell performances with different configurations are compared. The reduction of voltage demand for optimized flow field is 0.062V compared to traditional straight flow field. The enhancement of porous material flow field in anode is more evident when adopt this flow field on both sides of cell.

Acknowledgement

This work is supported by the National Key Research and Development Program of China (2017YFB0601904). M. Ni thanks the grant (Project Number: PolyU 152214/17E) from Research Grant Council, University Grants Committee, Hong Kong SAR.

References

[1] Guo S, Liu Q, Sun J, et al. A review on the utilization of hybrid renewable energy. Renewable and Sustainable Energy Reviews, 2018, 91: 1121-1147.

[2] Yang Y, Bremner S, Menictas C, et al. Battery energy storage system size determination in renewable energy systems: A review. Renewable and Sustainable Energy Reviews, 2018, 91: 109-125.

[3] Luo Y, Wu X, Shi Y, et al. Exergy analysis of an integrated solid oxide electrolysis cell-methanation reactor for renewable energy storage. Applied Energy, 2018, 215: 371-383.

[4] Jensen S H, Graves C, Mogensen M, et al. Large-scale electricity storage utilizing

reversible solid oxide cells combined with underground storage of CO2 and CH4. Energy & Environmental Science, 2015, 8(8): 2471-2479.

[5] Zhang X, Song Y, Wang G, et al. Co-electrolysis of CO2 and H2O in high-temperature solid oxide electrolysis cells: Recent advance in cathodes. Journal of Energy Chemistry, 2017, 26(5): 839-853.

[6] Menon V, Fu Q, Janardhanan V M, et al. A model-based understanding of solid-oxide electrolysis cells (SOECs) for syngas production by H2O/CO2 co-electrolysis. Journal of Power Sources, 2015, 274: 768-781.

[7] Wen H, Ordonez J C, Vargas J V C. Optimization of single SOFC structural design for maximum power. Applied Thermal Engineering, 2013, 50(1): 12-25.

[8] Li W, Zhang Q, Wang C, et al. Experimental and numerical analysis of a three-dimensional flow field for PEMFCs. Applied Energy, 2017, 195: 278-288.

[9] El-Zoheiry R M, Ookawara S, Ahmed M. Efficient fuel utilization by enhancing the under-rib mass transport using new serpentine flow field designs of direct methanol fuel cells. Energy Conversion and Management, 2017, 144: 88-103.

[10] Wen H, Ordonez J C, Vargas J V C. Optimization of single SOFC structural design for maximum power. Applied Thermal Engineering, 2013, 50(1): 12-25.

[11] Liu H, Yang W, Tan J, et al. Numerical analysis of parallel flow fields improved by micro-distributor in proton exchange membrane fuel cells. Energy Conversion and Management, 2018, 176: 99-109.

[12] Yan X, Guan C, Zhang Y, et al. Flow field design with 3D geometry for proton exchange membrane fuel cells. Applied Thermal Engineering, 2019, 147: 1107-1114.

519 [13] Wang X D, Xu J L, Yan W M, et al. Transient response of PEM fuel cells with parallel
520 and interdigitated flow field designs. International Journal of Heat and Mass Transfer,
521 2011, 54(11-12): 2375-2386.
522 [14] Jiao K, Li X. Water transport in polymer electrolyte membrane fuel cells. Progress in
523 Energy and Combustion Science, 2011, 37(3): 221-291.
524 [15] Duhn J D, Jensen A D, Wedel S, et al. Optimization of a new flow design for solid oxide
525 cells using computational fluid dynamics modelling. Journal of Power Sources, 2016, 336:
526 261-271.
527 [16] Bi W, Chen D, Lin Z. A key geometric parameter for the flow uniformity in planar solid
528 oxide fuel cell stacks. International Journal of Hydrogen Energy, 2009, 34(9): 3873-3884.
529 [17] Lin B, Shi Y, Cai N. Numerical simulation of cell-to-cell performance variation within a
530 syngas-fuelled planar solid oxide fuel cell stack. Applied Thermal Engineering, 2017,
531 114: 653-662.
532 [18] Dong J, Xu X, Xu B. CFD analysis of a novel modular manifold with multi-stage
533 channels for uniform air distribution in a fuel cell stack. Applied Thermal Engineering,
534 2017, 124: 286-293.
535 [19] Qu Z, Aravind P V, Boksteen S Z, et al. Three-dimensional computational fluid dynamics
536 modeling of anode-supported planar SOFC. International Journal of Hydrogen Energy,
537 2011, 36(16): 10209-10220.
538 [20] Wei S S, Wang T H, Wu J S. Numerical modeling of interconnect flow channel design
539 and thermal stress analysis of a planar anode-supported solid oxide fuel cell stack. Energy,
540 2014, 69: 553-561.

[21] Lin Z, Stevenson J W, Khaleel M A. The effect of interconnect rib size on the fuel cell concentration polarization in planar SOFCs. Journal of Power Sources, 2003, 117(1):92-97.

[22] Zhang G, Jiao K. Multi-phase models for water and thermal management of proton exchange membrane fuel cell: A review. Journal of Power Sources, 2018, 391:120-133.

[23] Li X, Shi Y, et al. Optimization of interconnect flow channels width in a planar solid oxide fuel cell. International Journal of Hydrogen Energy, 2018, 43(46):13738-13750.

[24] Liu S, Song C, Lin Z. The effects of the interconnect rib contact resistance on the performance of planar solid oxide fuel cell stack and the rib design optimization. Journal of Power Sources, 2008, 183(1):214-225.

[25] Moreno-Blanco J, Elizalde-Blancas F, Riesco-Avila J M, et al. On the effect of gas channels-electrode interface area on SOFCs performance. International Journal of Hydrogen Energy, 2018.

[26] Hossain M S, Shabani B. Metal foams application to enhance cooling of open cathode polymer electrolyte membrane fuel cells. Journal of Power Sources, 2015, 295: 275-291.

[27] Tseng C J, Tsai B T, Liu Z S, et al. A PEM fuel cell with metal foam as flow distributor. Energy Conversion and Management, 2012, 62: 14-21.

[28] Afshari E, Houreh N B. Performance analysis of a membrane humidifier containing porous metal foam as flow distributor in a PEM fuel cell system. Energy conversion and management, 2014, 88: 612-621.

[29] Vazifeshenas Y, Sedighi K, Shakeri M. Heat transfer in PEM cooling flow field with high porosity metal foam insert. Applied Thermal Engineering, 2019, 147: 81-89.

563 [30] Zielke P, Wulff A C, Sun X, et al. Investigation of a Spinel-forming Cu-Mn Foam as an
564 Oxygen Electrode Contact Material in a Solid Oxide Cell Single Repeating Unit. Fuel
565 Cells, 2017, 17(5).
566 [31] Luo Y, Shi Y, Li W, et al. Dynamic electro-thermal modeling of co-electrolysis of steam
567 and carbon dioxide in a tubular solid oxide electrolysis cell. Energy, 2015, 89: 637-647.
568 [32] Andersson M, Yuan J, Sundén B. SOFC modeling considering electrochemical reactions
569 at the active three phase boundaries. International Journal of Heat and Mass Transfer,
570 2012, 55(4): 773-788.
571 [33] Mu D, Liu Z S, Huang C, et al. Determination of the effective diffusion coefficient in
572 porous media including Knudsen effects. Microfluidics and Nanofluidics, 2008, 4(3):
573 257-260.
574 [34] Li W, Shi Y, Luo Y, et al. Elementary reaction modeling of solid oxide electrolysis cells:
575 Main zones for heterogeneous chemical/electrochemical reactions. Journal of Power
576 Sources, 2015, 273: 1-13.
577 [35] Fuller E N, Schettler P D, Giddings J C. New method for prediction of binary gas-phase
578 diffusion coefficients. Industrial & Engineering Chemistry, 1966, 58(5): 18-27.
579 [36] Ni M. Modeling and parametric simulations of solid oxide fuel cells with methane carbon
580 dioxide reforming. Energy Conversion and Management, 2013, 70: 116-129.
581 [37] Haberman B A, Young J B. Three-dimensional simulation of chemically reacting gas
582 flows in the porous support structure of an integrated-planar solid oxide fuel cell.
583 International Journal of Heat and Mass Transfer, 2004, 47(17-18): 3617-3629.
584 [38] Pan Z, Liu Q, Zhang L, et al. Experimental and thermodynamic study on the performance

585 of water electrolysis by solid oxide electrolyzer cells with Nb-doped Co-based perovskite
586 anode. Applied Energy, 2017, 191: 559-567.
587 [39] Stempien J P, Sun Q, Chan S H. Performance of power generation extension system
588 based on solid-oxide electrolyzer cells under various design conditions. Energy, 2013, 55:
589 647-657.
590 [40] Gholaminezhad I, Paydar M H, Jafarpur K, et al. Multi-scale mathematical modeling of
591 methane-fueled SOFCs: Predicting limiting current density using a modified Fick's
592 model. Energy Conversion and Management, 2017, 148: 222-237.
593 [41] Tang S, Amiri A, Vijay P, et al. Development and validation of a computationally
594 efficient pseudo 3D model for planar SOFC integrated with a heating furnace. Chemical
595 Engineering Journal, 2016, 290: 252-262.
596 [42] Hussain M M, Li X, Dincer I. A general electrolyte‐electrode-assembly model for the
597 performance characteristics of planar anode-supported solid oxide fuel cells. Journal of
598 Power Sources, 2009, 189(2): 916-928.
599 [43] Andersson M, Yuan J, Sundé n B. SOFC modeling considering hydrogen and carbon
600 monoxide as electrochemical reactants. Journal of Power Sources, 2013, 232: 42-54.
601 [44] Janardhanan V M, Deutschmann O. CFD analysis of a solid oxide fuel cell with internal
602 reforming: Coupled interactions of transport, heterogeneous catalysis and electrochemical
603 processes. Journal of Power Sources, 2006, 162(2): 1192-1202.
604 [45] Du Y, Qin Y, Zhang G, et al. Modelling of effect of pressure on co-electrolysis of water
605 and carbon dioxide in solid oxide electrolysis cell. International Journal of Hydrogen
606 Energy, 2019, 44(7): 3456-3469.

[46] Menon V, Janardhanan V M, Deutschmann O. A mathematical model to analyze solid oxide electrolyzer cells (SOECs) for hydrogen production. Chemical Engineering Science, 2014, 110: 83-93.